Mechanism and Machine Theory 210 (2025) 106016

Contents lists available at ScienceDirect

Mechanism and Machine Theory

journal homepage: www.elsevier.com/locate/mechmt

Research paper

Cable-driven parallel robot trajectory generation with optimized orientation considering disturbance rejection

Shuai Liu [a], Molong Duan [a,b,*]

[a] Department of Mechanical and Aerospace Engineering, The Hong Kong University of Science and Technology, Hong Kong SAR, PR China
[b] HKUST Shenzhen-Hong Kong Collaborative Innovation Research Institute, Futian, Shenzhen, PR China

ARTICLE INFO

Keywords:
Cable-driven parallel robots
Disturbance rejection
Additive manufacturing
Trajectory generation
Orientation optimization

ABSTRACT

Cable-driven parallel robots are desirable for large-scale manipulation tasks due to their low inertia, low cost, high speed, high flexibility, and high energy efficiency. Such tasks are typically performed outdoors, which requires the robot to have enhanced disturbance rejection capability. In this work, the disturbance rejection is achieved by exploiting the robot's redundancy in tasks where the end effector orientations are not strictly constrained (e.g., additive manufacturing). Exploiting this orientation redundancy, an anti-disturbance trajectory generator is proposed for cable-driven parallel robots based on a variation-based disturbance rejection function and an optimization with orientation as the variable. The performance of the proposed trajectory generation method is verified with a cable-driven parallel 3D printer to show enhanced stiffness and tracking performance under gust conditions in simulations and experiments.

1. Introduction

Cable-driven parallel mechanisms are increasingly exploited in applications that require large-scale manipulations [1], such as construction equipment [2], large-scale telescopes [3], inventory systems [4], stadium camera systems [5], and rehabilitation systems [6,7]. Cable-driven parallel robot (CDPR), in contrast to rigid serial robots, offers the benefits of low inertia [8], high speed [9], high payload capacity [10], large reachable workspace [11], and reconfigurability [12]. The CDPR can maneuver the end effector (EE) to arbitrary locations in the workspace without pre-constructed guideways or gantry systems, thus reducing the setup time and construction cost [13]. The mechanisms of CDPR mitigate the accumulation of errors from different degrees of freedom (DOFs) due to the parallel mechanism, enabling precise positioning in large workspaces [14].

The CDPR's potential application in large-scale manipulation in outdoor environments may experience strong disturbances like gusts [15]. The gust loading of a CDPR must be explicitly considered to account for the limited stiffness and strength of the cables [16]. Accordingly, disturbance rejection capabilities are crucial for industrial CDPR manipulation [17]. Lack of disturbance rejection capability may lead to manipulation inaccuracy, mechanism failure, and even safety hazards. The disturbance rejection capabilities of CDPR are currently evaluated under static and dynamic stiffness analysis paradigms [18], upon which various mechatronics approaches has been established. Gueners et al. [19] and Anson et al. [20] designed several CDPR anchor point adjustment devices and corresponding optimization algorithms to control cable preload to affect overall stiffness. Similarly, Su et al. [5] introduced a pulley position adjustment device to optimize CDPR gust rejection capability. Yeo et al. [21] proposed attaching a variable-stiffness device

* Corresponding author.
E-mail address: duan@ust.hk (M. Duan).

https://doi.org/10.1016/j.mechmachtheory.2025.106016
Received 11 December 2024; Received in revised form 20 March 2025; Accepted 24 March 2025
Available online 4 April 2025

along each driving cable to adjust the stiffness of the CDPR to account for the requirements of different tasks, such as outdoor large-scale applications and robot-human cooperation. In addition, Cuvillon et al. [22] introduced several on-board propellers to improve CDPR disturbance rejection capability. However, these mechatronics-enabled approaches require additional real-time control system, actuators and sensors, and thus may not be applied to general CDPR systems.

Besides the mechatronics-enabled approaches, other investigations into disturbance rejection have been focused on the CDPR design, trajectory generation, and control strategies. Cui et al. [23] optimized the dimension and shape of the anchor point configurations and EE for maximal constant stiffness space (CSS) volume. Jamshidifar et al. [24] decoupled the vibration model of a CDPR to form a linear parametric varying dynamic system under the H-infinity control framework. They established a vibration compensator for kinematically constrained redundant CDPR with improved stiffness. Yang et al. [25] proposed an isotropic control framework for CDPR to achieve effective vibration isolation uniformly in all directions. Qin et al. [26] introduced an adaptive recursive sliding mode control that combines adaptive disturbance observers with sliding mode control to enhance the system's robustness against uncertainties and disturbances. While such approaches are effective for improving trajectory tracking in CDPRs, they primarily focus on controller-level improvements and do not fully exploit the inherent redundancy in EE orientation.

Recent investigations [27] have pointed out that CDPRs are frequently designed to be over-actuation systems. The commonly seen over-actuation arises from the unconstrained EE orientation in many practical CDPR manipulation tasks. Additive manufacturing (AM) is an example of this over-actuation, as it only requires the printing nozzle to follow a specific trajectory without detailed constraints on the EE orientation [28]. This flexibility provides additional opportunities to exploit the EE orientation of CDPR to achieve optimal disturbance rejection capabilities, which have not been exploited in the existing work.

Motivated by the above research, an anti-disturbance trajectory generator (ADTG) is proposed to optimize EE orientations in CDPR trajectories, enhancing the system's disturbance rejection capabilities. The ADTG first evaluates the disturbance rejection capability by analyzing the effect of external disturbance on the tracking performance. Then, ADTG optimizes the disturbance rejection capability and generates the trajectory with optimal EE orientation. The proposed method can be applied in multiple disturbance conditions by designing the characteristic matrix.

To conclude, the core contributions of this paper are as follows:

- An analytical framework is established to evaluate the disturbance rejection capability and CDPR directional stiffness;
- An anti-disturbance trajectory generator is proposed to optimize the CDPR disturbance rejection by exploiting the EE orientation redundancy;
- The proposed trajectory generation method is verified in simulations and experiments on a CDPR prototype for AM that allows 6-DOF EE manipulation.

The paper is constructed as follows: The geometrical-based and tension-considering trajectory generation of a CDPR is detailed in Section 2. In Section 3, the CDPR disturbance rejection capability concerning orientations is first derived, followed by the introduction of the anti-disturbance trajectory generator. The detailed mechatronics design, simulation, and experiments are presented in Section 4, followed by the conclusion in Section 5.

2. CDPR trajectory generation with tension and error compensation

2.1. CDPR trajectory generation considering tension

Define an n-DOF CDPR, which is actuated with m cables. The geometry schematic of a conventional 6-DOF CDPR that allows the rotation of the EE is specified in Fig. 1. Define an inertial frame $\mathscr{F}_0$ fixed to the ground and a body-fixed frame $\mathscr{F}_B$ attached to the EE's center of gravity (CG). Vectors projected to $\mathscr{F}_B$ will be highlighted with superscript $^{(B)}$; other vectors are assumed to be projected to $\mathscr{F}_0$ by default. Assume m cables are attached to the anchor points $\mathbf{a}_1$, $\mathbf{a}_2$, $\dots\mathbf{a}_m$, where $\mathbf{a}_j \in \mathbb{R}^3$ are the coordinates in $\mathscr{F}_0$. The

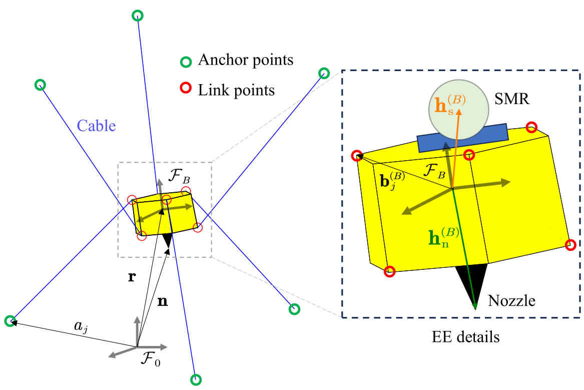

Fig. 1. Geometry schematic of a CDPR.

corresponding m link points on the EE are defined as $\mathbf{b}_1^{(B)}, \mathbf{b}_2^{(B)}, \ldots \mathbf{b}_m^{(B)}$, where $\mathbf{b}_j^{(B)} \in \mathbb{R}^3$ are their coordinates in $\mathscr{F}_B$. Define the CG's location as $\mathbf{r}$ projected into $\mathscr{F}_0$ and the Euler angles $\boldsymbol{\vartheta} = \{\psi,\ \theta,\ \phi\}^\top$ following the ZYX rotation sequence. The vector representing the cables from the EE link points to the anchor points $\mathbf{l}_j$ are defined as

$$\mathbf{l}_j = \mathbf{a}_j - \mathbf{r} - \underbrace{\mathbf{R}(\boldsymbol{\vartheta})\mathbf{b}_j^{(B)}}_{\mathbf{b}_j}, \tag{1}$$

where $\mathbf{R}(\boldsymbol{\vartheta})$ is the rotation matrix satisfying

$$\mathbf{R}(\boldsymbol{\vartheta}) = \begin{bmatrix} c_\psi c_\theta & c_\psi s_\theta s_\phi - s_\psi c_\phi & c_\psi s_\theta c_\phi + s_\psi s_\phi \\ s_\psi c_\theta & s_\psi s_\theta s_\phi + c_\psi c_\phi & s_\psi s_\theta c_\phi - c_\psi s_\phi \\ -s_\theta & c_\theta s_\phi & c_\theta c_\phi \end{bmatrix}, \tag{2}$$

where c_θ and s_θ are concise forms of $\cos(\theta)$ and $\sin(\theta)$. The unit directional vector is defined as

$$\mathbf{u}_j = \frac{\mathbf{l}_j}{L_j}, L_j = \| \mathbf{l}_j \|_2. \tag{3}$$

The most straightforward geometrical-based trajectory generation of the CDPR uses the length defined in (3) to actuate the individual motors. However, this method does not explicitly consider the limited stiffness of the cables. Therefore, it may lead to geometrical inaccuracy when the EE experiences excessive loads. This inaccuracy would be a severe issue when the CDPR is applied in manufacturing applications with disturbances (e.g., 3D printing) or outdoor environments with gusts. Therefore, this work considers the stiffness and load in commanding the trajectories of the individual motors. The forces of each cable $f_1, \ldots, f_m$ should statically satisfy

$$\underbrace{\begin{bmatrix} \mathbf{u}_1 & \cdots & \mathbf{u}_m \\ \mathbf{b}_1 \times \mathbf{u}_1 & \cdots & \mathbf{b}_m \times \mathbf{u}_m \end{bmatrix}}_{\mathbf{A}} \underbrace{\begin{Bmatrix} f_1 \\ \vdots \\ f_m \end{Bmatrix}}_{\mathbf{f}} + \underbrace{\begin{Bmatrix} \mathbf{f}_{\text{ext}} \\ \boldsymbol{\tau}_{\text{ext}} \end{Bmatrix}}_{\mathbf{w}} = \mathbf{0}, \tag{4}$$

where $\mathbf{f}_{ext}$ and $\boldsymbol{\tau}_{ext}$ are the external force and torque applied to the CG, projected to $\mathscr{F}_0$. Assuming linear elasticity, tension forces are further modeled as

$$\mathbf{f} = \mathbf{K}(\mathbf{L} - \mathbf{L}_0), \tag{5}$$

where $\mathbf{K} = \text{diag}\{k_1,\ k_2, \cdots, k_m\}$ is a diagonal stiffness matrix, $\mathbf{L}$ is the cable length with tension and $\mathbf{L}_0$ is the motor reference command representing cable length without tension, given by

$$\mathbf{L} = \{L_1, \cdots, L_m\}, \mathbf{L}_0 = \{L_{10}, \cdots, L_{m0}\}. \tag{6}$$

$\mathbf{L}$ and $\mathbf{L}_0$ are functions of the EE's location and orientation, which can be combined as a vector $\mathbf{p}$ and defined as

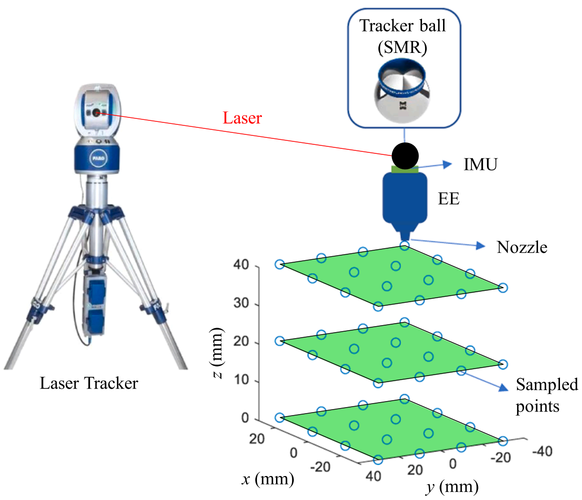

Fig. 2. Schematic of position error map measurement with laser tracker [29].

$$\mathbf{p} = \begin{Bmatrix} \mathbf{r} \\ \boldsymbol{\vartheta} \end{Bmatrix}. \tag{7}$$

To acquire a proper motor reference command $\mathbf{L}_0$ that considers the elongation because of tension, the static balance Eq. (4) is converted to

$$\mathbf{A}(\mathbf{p})\mathbf{K}(\mathbf{L}(\mathbf{p}) - \mathbf{L}_0(\mathbf{p})) + \mathbf{w} = \mathbf{0}. \tag{8}$$

Given an arbitrary spatial location and orientation $\mathbf{p}$, the geometrical length $\mathbf{L}(\mathbf{p})$ and effectiveness matrix $\mathbf{A}(\mathbf{p})$ is fixed. Therefore, the motor reference command $\mathbf{L}_0$ is given by

$$\mathbf{L}_0(\mathbf{p}) = \mathbf{L}(\mathbf{p}) + (\mathbf{A}(\mathbf{p})\mathbf{K})^{-1}\mathbf{w}. \tag{9}$$

This method of modifying the motor reference command based on the stiffness of the cable is referred to as the tension-considering method (TCM) in this paper.

2.2. CDPR trajectory generation with error compensation

To improve geometrical accuracy of CDPR, an error map is measured using a laser tracker and spherically mounted retroreflector (SMR), as shown in Fig. 2. The laser tracker measures only the translational position of the SMR, so an inertial measurement unit (IMU) is used to provide Euler angles of the EE $\boldsymbol{\vartheta}$ and transform the measurement to obtain the accurate location of the nozzle $\mathbf{r}_n$ in the global coordinate system given by

$$\mathbf{r}_n = \mathbf{r}_s + \mathbf{R}(\boldsymbol{\vartheta})\left(\mathbf{h}_n^{(B)} - \mathbf{h}_s^{(B)}\right), \tag{10}$$

where $\mathbf{r}_s$ is the location of the center of the SMR relative to the global coordinate system measured by the laser tracker, and $\mathbf{h}_s^{(B)}$ is the position of the SMR's center in the body-fixed frame $\mathscr{F}_B$, as illustrated in Fig. 1.

The compensation is built on an error map from the coordinates sampled as in Fig. 2. The coordinates of the points $\mathbf{r}_d$ to be measured are firstly designed to cover the workspace of the EE. Then, a G-code is generated, maneuvering the EE to the designated locations, and the nozzle location $\mathbf{r}_n$ is measured using the laser tracker. The corresponding positioning error at this point is given by

$$\mathbf{e} = \mathbf{r}_n - \mathbf{r}_d. \tag{11}$$

After visiting a sequence of points and acquiring its error, the error map of the workspace is generated. This error map is further interpolated for trajectory compensation in the future motion trajectory generated from the G-code. In the G-code, the reference is modified from $\mathbf{r}_d$ to $\mathbf{r}_d - \mathbf{e}$. While keeping the orientation unchanged, the position and orientation vector is recursively defined as

$$\mathbf{p}_{r,k} = \left\{\mathbf{r}_{d,k}{}^{\top}, \boldsymbol{\vartheta}^{\top}\right\}^{\top}, \mathbf{r}_{d,k} = \mathbf{r}_{d,k-1} - \mathbf{e}_k, \tag{12}$$

where $\mathbf{r}_{d,k}$ and $\mathbf{p}_{r,k}$ represent the compensated position and the combination of the position and orientation vector after k iterations, respectively; $\mathbf{e}_k$ is the error compensation vector measured in the k-th iteration. The initial condition satisfies $\mathbf{r}_{d,0} = \mathbf{r}_d$. After the k-th iteration, the cable reference command is generated with $\mathbf{p}_{r,k}$ representing $\mathbf{p}$ in (9), which can be expressed as

$$\mathbf{L}_0(\mathbf{p}_k) = \mathbf{L}(\mathbf{p}_k) + (\mathbf{A}(\mathbf{p}_k)\mathbf{K})^{-1}\mathbf{w}. \tag{13}$$

The iteration ends when the error $\mathbf{e}_k$ is less than the given tolerance. This method of changing the motor reference command based on cable stiffness and the error compensation is referred to in this paper as the tension-considering method with compensation (TCMC).

3. CDPR orientation optimization for disturbance rejection

3.1. Disturbance rejection capabilities of CDPR

Consider a CDPR EE with position and orientation given by $\mathbf{p}_0$, the external forces and moments of disturbances are decomposed into known and unknown parts:

$$\mathbf{w} = \mathbf{w}_0 + \delta\mathbf{w}, \tag{14}$$

where the known part $\mathbf{w}_0$ is typically due to gravity, while the unknown $\delta\mathbf{w}$ is typically from the disturbance force. Assuming that the cable length $\mathbf{L}$ is controlled following (4) with $\mathbf{w}$ replacing $\mathbf{w}_0$, the perturbed position and orientation are defined with $\mathbf{p}$ as follows

$$\mathbf{A}(\mathbf{p} + \delta\mathbf{p})\mathbf{K}(\mathbf{L}(\mathbf{p} + \delta\mathbf{p}) - \mathbf{L}_0(\mathbf{p})) + \mathbf{w} = \mathbf{0}. \tag{15}$$

Assume the disturbance $\delta\mathbf{w}$ is relatively small so as to enable the linear analysis. The linear relationship with the position and orientation perturbation $\delta\mathbf{p}$ is expressed as

$$\mathbf{A}(\mathbf{p})\mathbf{K}\frac{\partial \mathbf{L}}{\partial \mathbf{p}}\delta\mathbf{p} - \left(\frac{\partial \mathbf{A}}{\partial \mathbf{p}}\delta\mathbf{p}\right)\mathbf{A}(\mathbf{p})^{-1}\mathbf{w}_0 + \delta\mathbf{w} = \mathbf{0}. \tag{16}$$

The relationship between $\delta\mathbf{p}$ and $\delta\mathbf{w}$ can then be expressed as

$$\delta\mathbf{p} = \mathbf{D}(\mathbf{p})\delta\mathbf{w}, \tag{17}$$

where $\mathbf{D}(\mathbf{p})$ is the disturbance rejection matrix. The detailed calculation process from (15) to (16) is listed in Appendix A, and the determination process of disturbance rejection matrix is detailed in Appendix B,

3.2. Anti-disturbance trajectory generator based on CDPR orientation optimization

For applications of CDPRs where the nozzle position is crucial (e.g., AM), the orientation of the nozzle provides additional degrees of freedom for optimization. Consider using a CDPR for AM: define the position of the nozzle as $\mathbf{n} \in \mathbb{R}^3$ in $\mathscr{F}_0$ satisfying

$$\mathbf{n} = \mathbf{r} + \mathbf{R}(\boldsymbol{\vartheta})\mathbf{h}_n^{(B)}, \tag{18}$$

where $\mathbf{h}_n^{(B)}$ is the coordinates of the nozzle's position vector in the body-fixed frame $\mathscr{F}_B$, as illustrated in Fig. 1. The effect of disturbance on the nozzle position can be indirectly calculated with (17) and the geometrical relationship between $\mathbf{p}$ and $\mathbf{n}$. This is achieved by calculating the variation of (18) as

$$\delta\mathbf{n} = \underbrace{[\mathbf{I} \quad \mathbf{H}]}_{\triangleq \mathbf{E}(\mathbf{p})}\delta\mathbf{p}, \tag{19}$$

where $\mathbf{I}$ is an identity matrix and $\mathbf{H}$ is written as

$$\mathbf{H} = [\,\mathbf{t}_1 \times \mathbf{h}_\mathrm{n} \quad \mathbf{t}_2 \times \mathbf{h}_\mathrm{n} \quad \mathbf{t}_3 \times \mathbf{h}_\mathrm{n}\,]. \tag{20}$$

The term is calculated with $\mathbf{h}_n = \mathbf{R}(\boldsymbol{\vartheta})\mathbf{h}_n^{(B)}$. Combining (17) and (19), the disturbance to the nozzle position relationship is

$$\delta\mathbf{n} = \mathbf{E}(\mathbf{p})\mathbf{D}(\mathbf{p})\delta\mathbf{w}. \tag{21}$$

To establish a normalized form, the disturbance of the CDPR is mathematically defined as

$$\delta\mathbf{w} = \mathbf{D}_w f_d, \tag{22}$$

where f_d is the scalar representing the value of the disturbance force, and $\mathbf{D}_w \varepsilon \mathbb{R}^6 \mathrm{D_W} \varepsilon \mathrm{R}^6$ is the characteristic matrix, serving as a design weight and representing the effect of f_d on the CG. To evaluate the displacement of the nozzle, the norm of $\delta\mathbf{n}$ is calculated using a quadratic form:

$$|\delta\mathbf{n}|^2 = (\mathbf{E}(\mathbf{p})\mathbf{D}\mathbf{D}_w)^\top \mathbf{E}(\mathbf{p})\mathbf{D}\mathbf{D}_\mathrm{w} {f_d}^2. \tag{23}$$

Define a scalar-valued function to quantify the impact of external disturbances on the tracking performance as

$$f(\mathbf{p}) = (\mathbf{E}(\mathbf{p})\mathbf{D}\mathbf{D}_w)^\top \mathbf{E}(\mathbf{p})\mathbf{D}\mathbf{D}_w. \tag{24}$$

This function should have a sufficiently low value to enhance the disturbance rejection capability of the CDPR. Considering a specific nozzle position $\mathbf{n}$, the position and orientation of the EE are determined by

$$\mathbf{p} = \begin{Bmatrix} \mathbf{n} - \mathbf{h}_\mathrm{n} \\ \boldsymbol{\vartheta} \end{Bmatrix} = \mathbf{g}(\mathbf{n}, \boldsymbol{\vartheta}), \tag{25}$$

which suggests that $\mathbf{p}$ varies with the Euler angles adopted. Therefore, the objective becomes finding the minimum value of $f(\mathbf{p})$ by systematically adjusting the Euler angles at a given nozzle position so as to achieve optimal disturbance rejection capability for this position. Accordingly, $f(\mathbf{p})$ is expressed as a function of $\mathbf{n}$ and $\boldsymbol{\vartheta}$ by combining (24) and (25):

$$f(\mathbf{p}) = f(\mathbf{g}(\mathbf{n}, \boldsymbol{\vartheta})) = h(\mathbf{n}, \boldsymbol{\vartheta}). \tag{26}$$

For an unconstrained counterpart optimization problem to minimize $f(\mathbf{p})$, the optimized value should satisfy the first-order optimality condition defined as

$$\left.\frac{\partial h(\mathbf{n}, \boldsymbol{\vartheta})}{\partial \boldsymbol{\vartheta}}\right|_{\boldsymbol{\vartheta}=\boldsymbol{\vartheta}^*} = 2\mathbf{J}^\top(\overline{\mathbf{V}} - \mathbf{E}\mathbf{D}\overline{\mathbf{F}}\mathbf{E}_o) = \mathbf{0}, \tag{27}$$

where $\boldsymbol{\vartheta}^*(\mathbf{n})$ is defined as the optimal Euler angle considering disturbance rejection capability, and the column vectors in $\mathbf{E}_o$ are in the orthogonal complement of $\mathbf{E}$. $\mathbf{E}_o$ can be expressed as

$$\mathbf{E}_o = \frac{\partial \mathbf{p}}{\partial \boldsymbol{\vartheta}} = [\,-\mathbf{H} \quad \mathbf{I}\,]^\top. \tag{28}$$

Other terms in (27) are defined as

$$\mathbf{J} = \mathbf{E}(\mathbf{p})\mathbf{D}\mathbf{D}_w, \tag{29}$$

$$\overline{\mathbf{V}} = \sum_{i=1}^{6} \mathbf{V}_i(\mathbf{D}_i\mathbf{D}_w), \mathbf{V}_i = \frac{\partial \mathbf{H}}{\partial p_i}, \tag{30}$$

$$\overline{\mathbf{F}} = \sum_{i=1}^{6} \mathbf{F}_i(\mathbf{D}_i\mathbf{D}_w), \mathbf{F}_i = \frac{\partial \mathbf{C}}{\partial p_i}, \tag{31}$$

$$\mathbf{D} = [\mathbf{D}_1\ \mathbf{D}_2\ \mathbf{D}_3\ \mathbf{D}_4\ \mathbf{D}_5\ \mathbf{D}_6]^\top, \tag{32}$$

where $\mathbf{F}_i$ is obtained by calculating the derivative of each element of $\mathbf{C}$ regarding p_i under the Einstein summation protocol; the derivative of the inverse of $\mathbf{A}$ can be obtained by using the identity of an inverse's derivatives. Following this first-order optimality condition, a function $\mathbf{q}(\boldsymbol{\vartheta})$ is defined to represent the closeness of the Euler angle to the local minimum at a specific nozzle position, which is expressed as

$$\mathbf{q}(\boldsymbol{\vartheta}) = \mathbf{J}^\top(\overline{\mathbf{V}} - \mathbf{E}\mathbf{D}\overline{\mathbf{F}}\mathbf{E}_o). \tag{33}$$

With the disturbance rejection Euler angles optimized, an ADTG is established via parameterizing the representative optimization results (e.g., via a neural network) to formulate a continuous relationship $\boldsymbol{\vartheta}^*(\mathbf{n})$. This general nonlinear relationship provides the optimized position and orientation of the EE following

$$\mathbf{p}^* = \begin{Bmatrix} \mathbf{n} - \mathbf{R}(\boldsymbol{\vartheta}^*(\mathbf{n}))\mathbf{h}_n^{(B)} \\ \boldsymbol{\vartheta}^*(\mathbf{n}) \end{Bmatrix}. \tag{34}$$

The ADTG is an improvement based on TCMC. Compared to TCMC, ADTG keeps the nozzle position $\mathbf{n}$ unchanged to ensure positioning accuracy, while adjusting the orientation to enhance the CDPR's disturbance rejection capability during CDPR manipulation.

The realizations of the trajectory generation methods (TCMC and ADTG) in (12), and (34) rely on the modification of the kinematics calculation module, introducing additional parameters (e.g., stiffness) and input functions (error compensation map and optimal Euler angle function) to the original formulations. In practice, due to the complexity of solving the optimization problem listed in (27), it is more practical to perform the optimization using algorithms like particle swarm working in MATLAB to find the optimal Euler angle. For a given nozzle position $\mathbf{n}$, the optimal Euler angle that maximizes the disturbance rejection capability can be found via the optimization problem expressed as

$$\begin{aligned} &\min_{\boldsymbol{\vartheta}} \int\int\int_{\boldsymbol{\Omega}(\mathbf{n})} \lambda(\mathbf{n})h(\mathbf{n},\boldsymbol{\vartheta})dxdydz + \mu\|\ \boldsymbol{\vartheta}\ \|, \\ &\quad s.t. |\psi| \le \psi_{\max}, |\theta| \le \theta_{\max}, |\phi| \le \phi_{mas}, \end{aligned} \tag{35}$$

where $\boldsymbol{\Omega}(\mathbf{n})$ is the neighborhood spherical region around the nozzle position $\mathbf{n}$. The first term of the cost function is the integral form, which aims for the continuity of the optimized Euler angle over the region $\boldsymbol{\Omega}$, ensuring smooth transitions across neighboring points. In the integral term, $\lambda(\mathbf{n})$ serves as a weighting function of $h(\mathbf{n},\boldsymbol{\vartheta})$ within $\boldsymbol{\Omega}$. It assigns higher weights to points closer to the current nozzle position and lower weights to points farther away, ensuring a spatially localized emphasis. Additionally, $\lambda(\mathbf{n})$ is normalized following the Gaussian distribution such that its integral over the spherical region equals 1, preserving consistency in the overall contribution of the neighborhood. The second term includes μ, which is the weight of the norm of $\boldsymbol{\vartheta}$, balancing its influence in the cost function. Including limits on the norm $\boldsymbol{\vartheta}$ of within a certain range serves to prevent cable-EE interference and large tilt angles, which compromise the manufacturing performance. Note that the formula in (35) considers the constraints, optimization regularization, and results smoothing. In practical implementation of this optimization through coding, the triple integral in (35) is approximated by summing contributions from discrete sampling points within the region $\boldsymbol{\Omega}$, expressed as

$$\int\int\int_{\boldsymbol{\Omega}(\mathbf{n})} \lambda(\mathbf{n})h(\mathbf{n},\boldsymbol{\vartheta})dxdydz \approx \sum_i \lambda(\mathbf{n}_i)h(\mathbf{n}_i,\boldsymbol{\vartheta}) \tag{36}$$

where $\mathbf{n}_i$ represents a sampling point in $\boldsymbol{\Omega}$. The discrete weights $\lambda(\mathbf{n}_i)\lambda(\mathrm{n_i})$ are normalized such that their summation equals 1.

4. Simulation and experimental verifications

4.1. Cable-driven parallel robot design and prototype for AM

To verify the proposed methods, TCMC is chosen as the representative baseline for comparison with the ADTG method, as it similarly does not require additional actuators, sensors, specialized structures, or real-time control system. Also, a CDPR system for AM is designed and built, as illustrated in Fig. 3. The outer frame of the CDPR system has a 270mm $\times$ 460mm six-prismatic structure. More detailed information about the hardware setup is discussed in our previous conference paper [29]. A Bigtreetech Octopus mainboard runs the open-source 3D control firmware Klipper, which converts the G-code to cable length commands. In Klipper's inverse kinematics setup, the TCMC and proposed ADTG methods are implemented. In the optimization process of ADTG listed in (35), $\boldsymbol{\Omega}$ is defined as all sampling points within a 10 cm radius around $\mathbf{n}$, and μ is set to 0.0006 in our calculations.

A laptop (CPU: AMD Ryzen 55600H, GPU: NVIDIA RTX 3050) is utilized to precompute the optimal Euler angles, with a calculation time of approximately 30 s for each sampled point. After the optimal Euler angle is obtained for all the sampled points, a shallow neural network is utilized to fit a continuous function of the optimal Euler angle regarding the nozzle position to make it more implementable for the current mainboard setup. This fitted function computes the optimal Euler angle for each position in <1 millisecond, making it suitable for the printing process on the current mainboard setup. To verify the proposed ADTG method's enhancement of disturbance rejection, simulations of the CDPR's tracking performance under gusts and stiffness, experiments on tracking performance and printing performance under gusts are evaluated.

4.2. Simulation results on the disturbance rejection

To test the stiffness of the CDPR with the TCMC and ADTG methods, a simulation of the CDPR dynamics is established. Following the relationship of $\mathbf{p}$ and $\mathbf{n}$ in (18), the variation in the nozzle position can be evaluated. An external white-noise disturbance force with a mean value of 1 N is introduced from 0.5 s to simulate a stochastic gust. The disturbance is assumed to be unidirectional along the x-direction. The amplitude of the gust disturbance force is set to simulate the real-world environment. Two trajectory generation methods, the TCMC, as given in (12), and the proposed ADTG in (34), are exploited to generate the cable length command to compare its tracking performance under disturbance. To account for the x-direction disturbance, the characteristic matrix in the ADTG is designed to be

$$\mathbf{D}_w = \{1, 0, 0, 0, 0, 0\}^\top. \tag{37}$$

Note that this characteristic matrix $\mathbf{D}_w$ is selected considering practical scenarios where the gust directions are fixed (e.g., gaps between buildings). For those scenarios, characteristic matrix $\mathbf{D}_w$ is constant. For more complex environments with varying gust directions, the current characteristic matrix could schedule along the gust directions as long as the direction is predictable. The detailed simulation block diagram is shown in Fig. 4, where $\mathbf{K}$ denotes the stiffness of cables. The CDPR equation of motion (EOM) describes the relationship between the forces/torques and motion in (4), and $L(\mathbf{p})$ transfers the current position and orientation to the length of the cables.

The disturbance profile and tracking performance with the TCMC and the ADTG are shown in Fig. 5, where e_x, e_y, and e_z represent the positioning error in the x-, y-, and z-axis, respectively. It is clearly seen that the tracking accuracy without the disturbance before 0.5 s is almost the same for the TCMC and ADTG. However, with the disturbance introduced, the tracking error of ADTG is significantly smaller (about 6 % and 9 %) compared to the TCMC in the x and y directions. This preservation of position accuracy is crucial for AM applications as it directly contributes to the printed part's geometric features. The z-axis error is relatively small, mainly because the disturbance is from the horizontal direction and there is relatively high stiffness in the z-direction.

The stiffness of the CDPR has also been proven to be an effective indicator of disturbance rejection capability. To calculate the average directional stiffness, the workspace of the CDPR is sampled with a grid size of 10 mm; each sampled point's directional stiffness (including translational and rotational) is evaluated following (16). The average directional stiffness is summarized in Table 1.

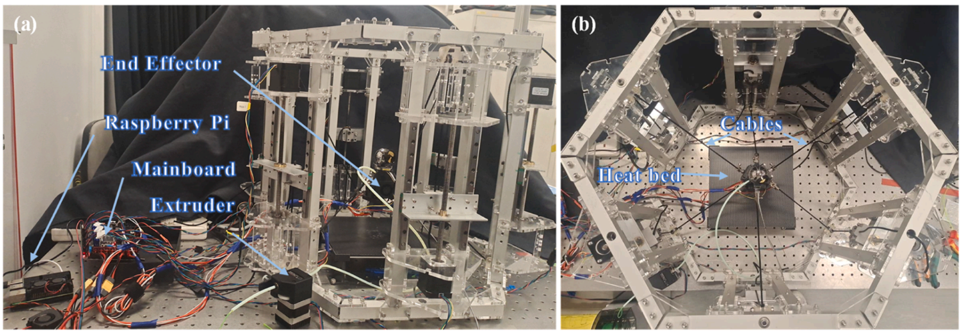

Fig. 3. (a) Overview and (b) top view of the cable-driven robot prototype for AM.

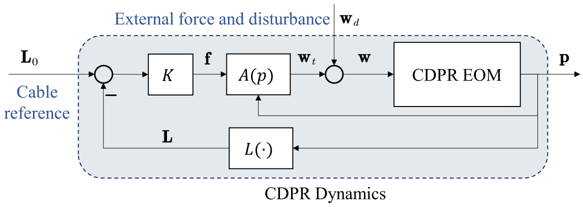

Fig. 4. The block diagram of CDPR dynamics.

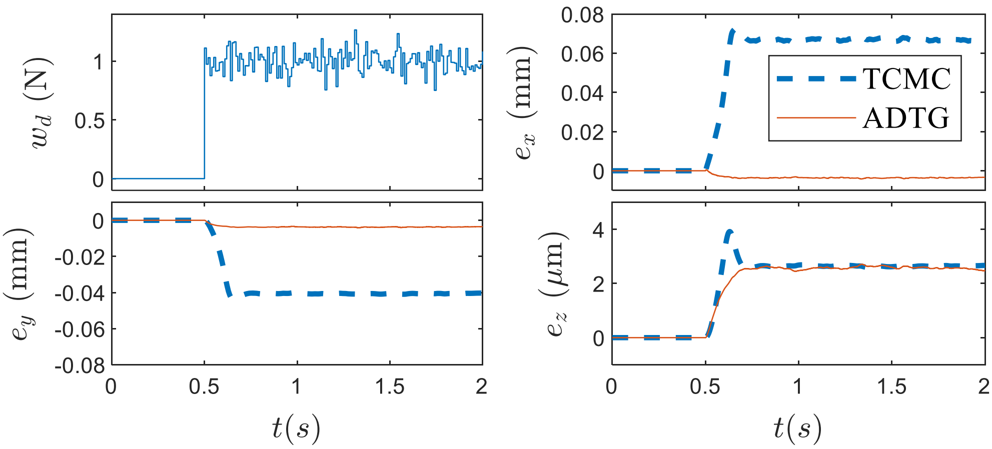

Fig. 5. Simulation of the nozzle position tracking under gusts with the TCMC and ADTG (proposed) methods.

Table 1
Average directional stiffness of CDPR with TCMC and ADTG methods.

Average stiffness	TCMC	ADTG	Enhancement
k_x (kN/m)	3.342	13.091	291.712 %
k_y (kN/m)	5.511	16.459	198.657 %
k_z (kN/m)	60.320	95.619	58.520 %
k_ϕ $(kN/^\circ)$	23.231	45.725	96.828 %
k_θ $(kN/^\circ)$	60.918	46.467	−23.72 %
k_ψ $(kN/^\circ)$	0.125	0.987	689.600 %

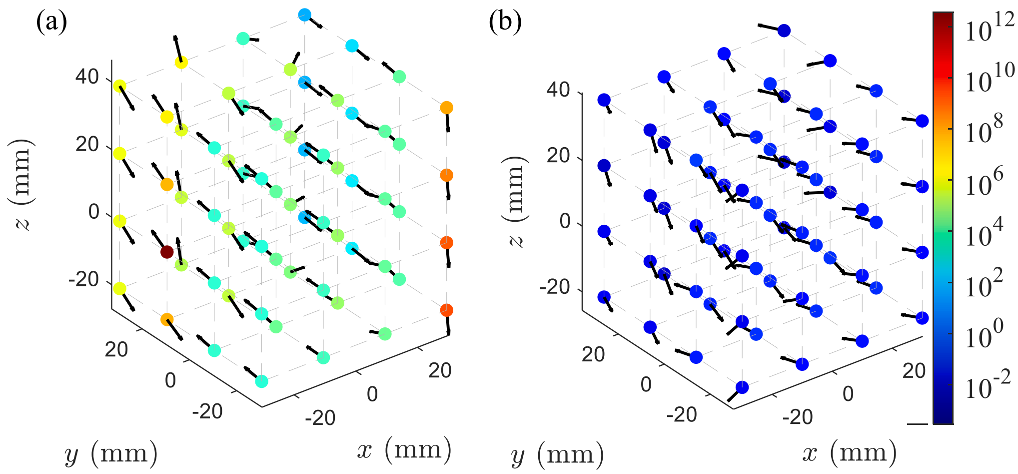

Fig. 6. The norm and directions of the $\mathbf{q}(\vartheta)$ vector in the workspace, indicating disturbance effectiveness with the (a) TCMC and (b) ADTG (proposed) methods.

It is observed that the directional stiffness of the ADTG has a significant increase compared to the TCMC in most translational and rotational directions. This increased stiffness indicates the CDPR's enhanced disturbance rejection capabilities. Note that the ADTG's k_θ direction has a slight decrease in stiffness. This mainly arises from the original high values of k_θ, which is balanced in the optimization procedures. k_θ has a relatively high value because the CDPR setup is not 90° rotational symmetrical in the x-y plane, making the stiffnesses around the x and y axes differ. The results show that the current characteristic matrix supports a certain level of scheduling to account for gust direction variations.

To further represent the distance between the current Euler angle and the optimal Euler angle considering the disturbance rejection capability, the distance to optimality metric $\mathbf{q}(\vartheta)$ in (33) is evaluated. The larger norm of $\mathbf{q}(\vartheta)$ indicates that the adopted Euler angle is farther from optimality. The corresponding norms and direction of $\mathbf{q}(\vartheta)$ with the TCMC and ADTG are shown in Fig. 6. It can be seen that the direction of $\mathbf{q}(\vartheta)$ is relatively random, while the norm of $\mathbf{q}(\vartheta)$ with the ADTG is at least six orders of magnitude smaller compared to the TCMC, indicating its enhanced disturbance rejection capability. Furthermore, the increase in the x translational direction is relatively high compared with other directions, mainly due to the fact that the stiffness is intentionally optimized for the x direction.

4.3. Printing performance comparison under gust disturbance

To experimentally measure the tracking performance of the CDPR with the ADTG and TCMC, the corresponding trajectories are generated to print a 3 mm × 10 mm × 5 mm cuboid with the same disturbance condition: x-direction gust disturbances with an average speed of 12.4 m/s (around Beaufort wind Level 6). A schematic of the setup is shown in Fig. 7. Note that in the lab configuration, the gust is relatively small. Baffles have been introduced to amplify the gust-induced disturbance to a sufficient level. The gust speed and the gust-induced force are measured using an anemometer and an additional load cell, respectively. The relationship between these two quantities is shown in Fig. 8. It is clear that the force increases with the gust speed, and the overall disturbance force reaches about 0.6 N with the predefined gust speed.

The tracking performance in the first 18 s after the gust's introduction is measured with a laser tracker; the results are plotted in Fig. 9 and summarized in Table 2. The experimental results agree with the simulation in that the tracking performances of the TCMC and ADTG methods are on the same level without the disturbance, while the ADTG method is capable of maintaining the tracking performance in the gust-affected regions. Note that oscillation at around 14 s is due to the sudden stoppage of the gust source, causing a step excitation and subsequent oscillation. The tracking errors of the TCMC and ADTG don't return to zero after gust disturbance is eliminated due to system errors and stepper motor step loss under high loads. The overall x-direction tracking error with the ADTG in the gust-affected regions is 86.3 % smaller compared to the TCMC in the dominant gust direction. Despite the characteristic matrix design not explicitly optimizing for the other directions, the tracking error is measured to have about a 70 % reduction when adopting ADTG. This aligns with the average directional stiffness of the CDPR with the TCMC and ADTG methods shown in Table 1 and the analysis that the ADTG enhances the general stiffness in almost all directions shown in Fig. 6.

The nozzle maintains a consistent vertical downward orientation throughout the entire printing process with TCMC. In contrast, the ADTG method demonstrates dynamic adjustments in nozzle orientation, which enhances the CDPR's resistance to disturbances. Fig. 10 illustrate the differences in nozzle orientation during the 3D printing process between the TCMC and ADTG methods. As the figure shows, the ADTG shows orientation changes in the roll direction compared to the TCMC. The actual printing results under gust disturbances are shown in Fig. 11. Gusts are introduced after printing the first 20 layers (bottom 1.2 mm). The overall gust-induced tracking error and its corresponding surface quality degradation are measured via a Keyence LJ-V73002D laser profiler. The ADTG approach's superior surface quality compared to the TCMC is illustrated in the lower part of Fig. 11. The root mean square error for the gust-facing surface is 0.3857 mm for the TCMC, and 0.0928 mm for the ADTG, indicating a 75.9 % enhancement in surface quality.

5. Conclusion

This work exploits the orientation redundancy in a cable-driven parallel robot (CDPR) to achieve enhanced disturbance rejection. The proposed method applies to CDPR manipulation where a strictly constrained orientation is absent, such as additive manufacturing. In contrast to conventional trajectory generation methods with geometrical information, tension, and other experimental error compensation, this paper systematically analyzes the disturbance rejection performance of a CDPR in different end effector orientations. Among the various orientations that satisfy the task requirements, an anti-disturbance trajectory is generated with an optimization problem that has the clustered disturbance rejection capability as the objective. Different trajectory generation method (TCMC) is compared with the proposed anti-disturbance trajectory generator (ADTG) in simulations and experiments. Enhanced disturbance rejection capabilities with the ADTG are illustrated in dynamic simulations and 3D printing experiments with gust disturbance.

Declaration of generative AI and AI-assisted technologies in the writing process

ChatGPT and Grammarly AI were used in the writing process only to perform grammar checks. After using these tools, the authors reviewed and edited the content, and take full responsibility for its publication.

CRediT authorship contribution statement

Shuai Liu: Writing – review & editing, Writing – original draft, Visualization, Validation, Software, Methodology, Data curation,

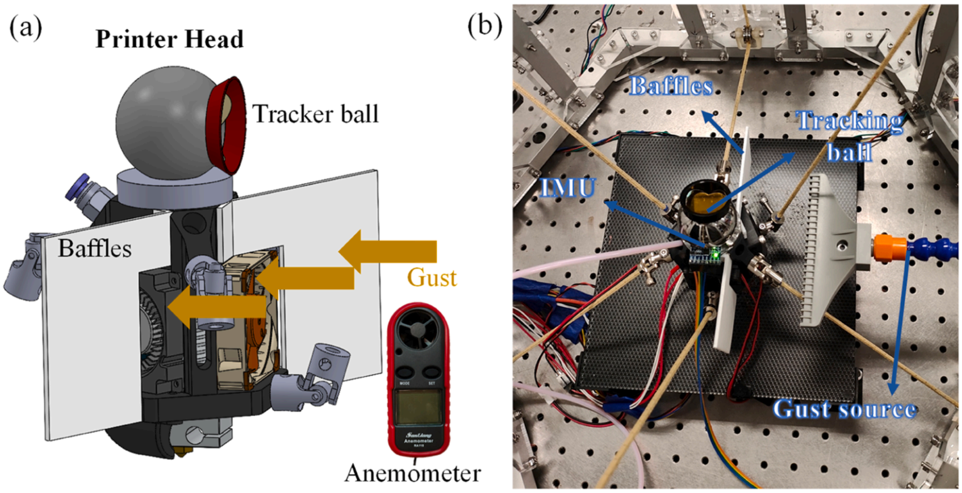

Fig. 7. (a) Schematic and (b) actual setup of 3D printing with gust disturbance.

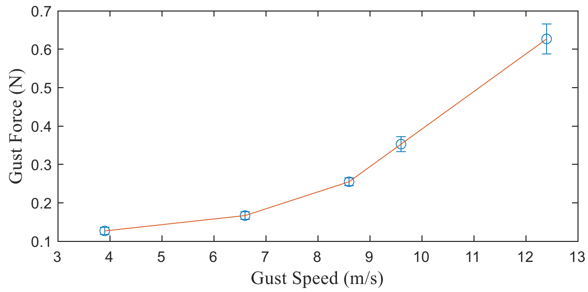

Fig. 8. Relationship between the gust speed and the disturbance force and its variation based on experiments.

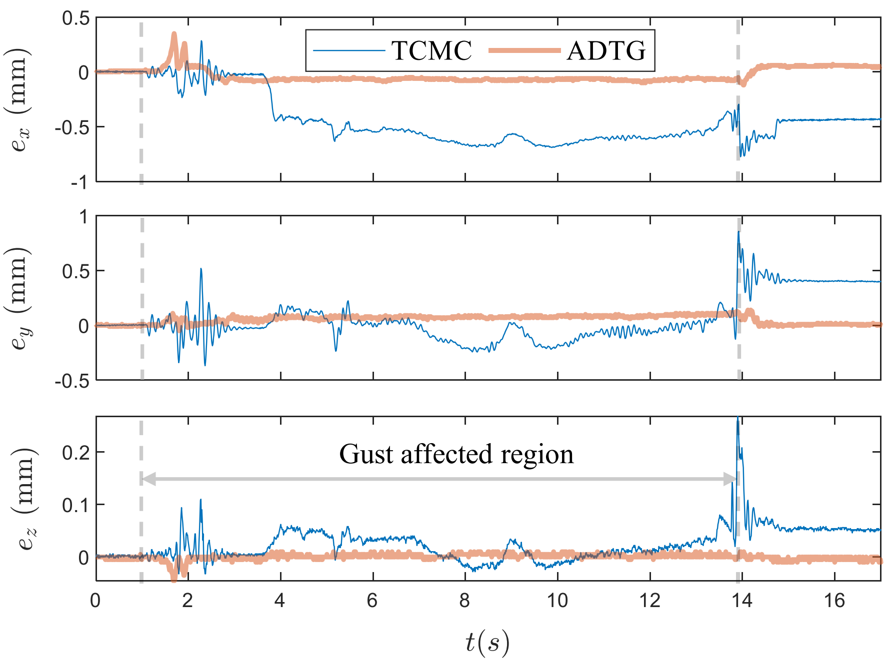

Fig. 9. Tracking error of the CDPR system with the TCMC and ADTG (proposed) methods.

Table 2
Tracking error of TCMC and ADTG when printing a line under a unidirectional gust.

RMS	e_x (mm)	e_y (mm)	e_z (mm)
TCMC	0.490	0.210	0.040
ADTG	0.067	0.065	0.012
Reduced ratio	86.3 %	69.0 %	70.0 %

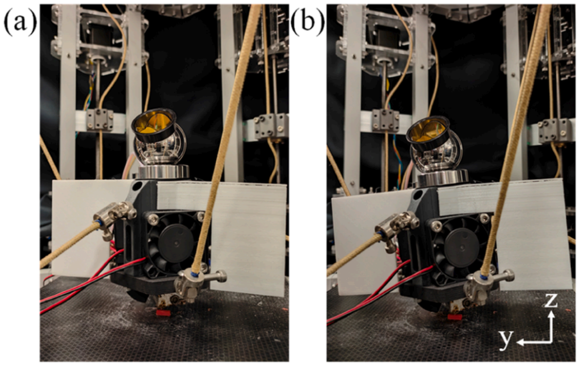

Fig. 10. 3D printing process with (a) TCMC and (b) ADTG.

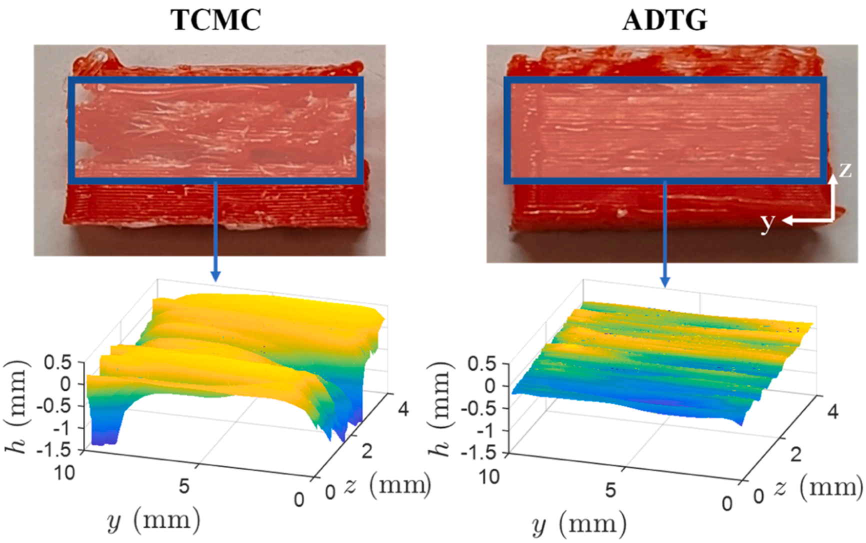

Fig. 11. The 3D printed parts under gust disturbances and their surface measurements, with the TCMC and ADTG (proposed) methods.

Conceptualization. **Molong Duan:** Writing – review & editing, Writing – original draft, Supervision, Resources, Project administration, Methodology, Funding acquisition, Conceptualization.

Declaration of competing interest

The authors declare that they have no known competing financial interests or personal relationships that could have appeared to influence the work reported in this paper.

Acknowledgements

This work was supported by the Frontier Technology Research for Joint Institutes with Industry Scheme under grant OKT24EG07, the Research Grants Council (RGC) of the Government of Hong Kong Special Administrative Region (HKSAR) with RGC/ECS Project No. 26215824, and the Innovation and Technology Commission (ITC) of the HKSAR with the ITF Project No. GHP/170/22SZ. The authors would like to thank Mr. Cheuk Hei Lam, Chin Fung Chan, King Hei (Adrian) Ho, Kin Ho (Leo) Liao, and Jiaquan Feng for their preliminary investigation into the CDPR setup, as well as Tania Leigh Wilmshurst for proofreading assistance.

Supplementary materials

Supplementary material associated with this article can be found, in the online version, at doi:10.1016/j.mechmachtheory.2025.106016.

Appendix A: Linear Parameter Variance Relationship between Disturbance and the Perturbation of Position and Orientation

Recalling (15),the perturbed position and orientation under disturbance follows:

$$\mathbf{A}(\mathbf{p}+\delta\mathbf{p})\mathbf{K}(\mathbf{L}(\mathbf{p}+\delta\mathbf{p})-\mathbf{L}_0(\mathbf{p}))+\mathbf{w}_0+\delta\mathbf{w}=\mathbf{0}. \tag{A.1}$$

Omitting the high-order derivatives, eq. (A.1) can be expanded as

$$\left(\mathbf{A}(\mathbf{p})+\frac{\partial\mathbf{A}}{\partial\mathbf{p}}\delta\mathbf{p}\right)\mathbf{K}\left(\mathbf{L}(\mathbf{p})+\frac{\partial\mathbf{L}}{\partial\mathbf{p}}\delta\mathbf{p}-\mathbf{L}_0(\mathbf{p})\right)+\mathbf{w}_0+\delta\mathbf{w}=\mathbf{0}, \tag{A.2}$$

where the tensor notation is following [30]. Note that

$$\mathbf{L}_0(\mathbf{p})=\mathbf{L}(\mathbf{p})+(\mathbf{A}(\mathbf{p})\mathbf{K})^{-1}\mathbf{w}, \tag{A.3}$$

equation (A.2) can be rewritten as

$$\left(\mathbf{A}(\mathbf{p})+\frac{\partial\mathbf{A}}{\partial\mathbf{p}}\delta\mathbf{p}\right)\mathbf{K}\left(\mathbf{L}(\mathbf{p})+\frac{\partial\mathbf{L}}{\partial\mathbf{p}}\delta\mathbf{p}-\mathbf{L}(\mathbf{p})-(\mathbf{A}(\mathbf{p})\mathbf{K})^{-1}\mathbf{w}_0\right)+\mathbf{w}_0+\delta\mathbf{w}=\mathbf{0}. \tag{A.4}$$

Simplify (A.4) and get the linear relationship between disturbance and the perturbation of position and orientation stated as:

$$\mathbf{A}(\mathbf{p})\mathbf{K}\frac{\partial\mathbf{L}}{\partial\mathbf{p}}\delta\mathbf{p}-\left(\frac{\partial\mathbf{A}}{\partial\mathbf{p}}\delta\mathbf{p}\right)\mathbf{A}(\mathbf{p})^{-1}\mathbf{w}_0+\delta\mathbf{w}=\mathbf{0}. \tag{A.5}$$

Appendix B: Disturbance Rejection Matrix Derivation

This relationship in tensor format with the Einstein summation protocol is written as

$$\delta w_i=\underbrace{\left(\frac{\partial A_{ij}}{\partial_{pk}}A_{or}{}^{-1}w_{0,r}-A_{ij}K_{jo}\frac{\partial L_o}{\partial_{pk}}\right)}_{\triangleq C_{ik}}\delta_{pk}, \tag{B.1}$$

where C_{ik} is a function of $\mathbf{p}$ and the matrix form is written as

$$\delta\mathbf{w}=\mathbf{C}(\mathbf{p})\delta\mathbf{p}. \tag{B.2}$$

Note that $\mathbf{C}(\mathbf{p})\in\mathbb{R}^{6\times6}$, regardless of the number of cables. Given that the rank of matrix $\mathbf{A}$ is 6, as well as the rank of matrix $\partial\mathbf{L}/\partial\mathbf{p}$, it can be assumed that matrix $\mathbf{C}$ is of full rank. The inversion of $\mathbf{C}(\mathbf{p})$ is defined as $\mathbf{D}(\mathbf{p})=\mathbf{C}(\mathbf{p})^{-1}$, yielding

$$\delta\mathbf{p}=\mathbf{D}(\mathbf{p})\delta\mathbf{w}. \tag{B.3}$$

Define $\mathbf{u}=[\mathbf{u}_1,\cdots,\mathbf{u}_m]$, $\mathbf{b}=[\mathbf{b}_1,\cdots,\mathbf{b}_m]$, and $\mathbf{l}=[\mathbf{l}_1,\cdots,\mathbf{l}_m]$. The partial derivatives of $\mathbf{A}$ and $\mathbf{L}$ regarding $\mathbf{p}$ are given by

$$\frac{\partial u_{ij}}{\partial r_k}=\frac{l_{kj}l_{ij}}{L_j{}^3}-\frac{\delta_{ik}}{L_j},\frac{\partial u_{ij}}{\partial\vartheta_k}=\sum_{n=1}^{3}\frac{\partial u_{ij}}{\partial b_{nj}}\frac{\partial b_{nj}}{\partial\vartheta_k}, \tag{B.4}$$

where δ_{ik} is the Kronecker delta. Similarly,

$$\frac{\partial u_{ij}}{\partial b_{nj}}=\frac{l_{nj}l_{ij}}{L_j{}^3}-\frac{\delta_{in}}{L_j}. \tag{B.5}$$

Note that $\partial b_{nj}/\partial r_k=0$. The partial derivative of the last three rows of $\mathbf{A}$ requires the calculation of the following terms:

$$\frac{\partial(\mathbf{b}_j \times \mathbf{u}_j)_i}{\partial r_k} = \sum_{m=1}^{3}\sum_{n=1}^{3} \varepsilon_{mni} b_{mj} \frac{\partial u_{nj}}{\partial r_k}, \tag{B.6}$$

$$\frac{\partial(\mathbf{b}_j \times \mathbf{u}_j)_i}{\partial \vartheta_k} = \sum_{m=1}^{3}\sum_{n=1}^{3} \varepsilon_{mni} \left(u_{nj} \frac{\partial b_{mj}}{\partial \vartheta_k} + b_{mj} \frac{\partial u_{nj}}{\partial \vartheta_k} \right), \tag{B.7}$$

where ε_{mni} is the alternating tensor defined as

$$\varepsilon_{mni} = \begin{cases} 1 & \textit{if } mni = 123, 312 \textit{ or } 231 \\ -1 & \textit{if } mni = 321, 132 \textit{ or } 213 \\ 0 & \qquad \textit{otherwise} \end{cases}. \tag{B.8}$$

The term $\partial b_{nj} / \partial \vartheta_k$ is conveniently constructed with

$$\frac{\partial \mathbf{b}_j}{\partial \vartheta_k} = \frac{\partial \mathbf{R}(\boldsymbol{\vartheta})}{\partial \vartheta_k} \mathbf{b}_j^{(B)} = \mathbf{t}_k \times \mathbf{b}_j, \tag{B.9}$$

where $\mathbf{t} = [\mathbf{t}_1 \quad \mathbf{t}_2 \quad \mathbf{t}_3]$, satisfying

$$\boldsymbol{\omega} = \underbrace{\begin{bmatrix} 0 & -S_\psi & C_\psi C_\theta \\ 0 & C_\psi & S_\psi C_\theta \\ 1 & 0 & -S_\theta \end{bmatrix}}_{\mathbf{t}} \dot{\boldsymbol{\vartheta}}. \tag{B.10}$$

The partial derivatives of $\mathbf{L}$ are decomposed to

$$\frac{\partial L_j}{\partial r_k} = -\frac{l_{kj}}{L_j}, \tag{B.11}$$

$$\frac{\partial L_j}{\partial \vartheta_k} = \frac{\partial L_j}{\partial b_j} \frac{\partial b_j}{\partial \vartheta_k} = -\frac{l_j^\top}{L_j} \mathbf{t}_k \times \mathbf{b}_j. \tag{B.12}$$

With (B.4)-(B.12), all elements in $\mathbf{C}(\mathbf{p})$ and the corresponding disturbance rejection matrix $\mathbf{D}(\mathbf{p})$ are acquired.

Data availability

Data will be made available on request.

References

[1] S. Qian, B. Zi, W.-W. Shang, Q.-S. Xu, A review on cable-driven parallel robots, Chinese J Mech Eng 31 (2018) 66, https://doi.org/10.1186/s10033-018-0267-9.

[2] T. Bruckmann, R. Boumann, Simulation and optimization of automated masonry construction using cable robots, Adv Eng Informatics 50 (2021) 101388, https://doi.org/10.1016/j.aei.2021.101388.

[3] R. Nan, D. Li, C. Jin, Q. Wang, L. Zhu, W. Zhu, et al., The five-hundred-meter aperture spherical radio telescope (FAST) project, Int J Mod Phys D 20 (2011) 989–1024.

[4] B. Salah, O. Janeh, B. Noche, T. Bruckmann, S. Darmoul, Design and simulation based validation of the control architecture of a stacker crane based on an innovative wire-driven robot, Robot Comput Integr Manuf 44 (2017) 117–128, https://doi.org/10.1016/j.rcim.2016.08.010.

[5] Y. Su, Y. Qiu, P. Liu, J. Tian, Q. Wang, X. Wang, Dynamic modeling, workspace analysis and multi-objective structural optimization of the large-span high-speed cable-driven parallel camera robot, Machines 10 (2022), https://doi.org/10.3390/machines10070565.

[6] C. Yang, J. Zhao, L. Li, S.K. Agrawal, Design and implementation of a novel modal space active force control concept for spatial multi-DOF parallel robotic manipulators actuated by electrical actuators, ISA Trans 72 (2018) 273–286, https://doi.org/10.1016/j.isatra.2017.10.006.

[7] N.S. Seyfi, A. Keymasi Khalaji, Robust control of a cable-driven rehabilitation robot for lower and upper limbs, ISA Trans 125 (2022) 268–289, https://doi.org/10.1016/j.isatra.2021.07.016.

[8] M. Zarebidoki, J.S. Dhupia, W. Xu, A review of cable-driven parallel robots: typical configurations, analysis techniques, and control methods, IEEE Robot Autom Mag 29 (2022) 89–106, https://doi.org/10.1109/MRA.2021.3138387.

[9] S. Kawamura, H. Kino, C. Won, High-speed manipulation by using parallel wire-driven robots, Robotica 18 (2000) 13–21, https://doi.org/10.1017/S0263574799002477.

[10] Pott A., Mütherich H., Kraus W., Schmidt V., Miermeister P., Verl A. IPAnema: A family of cable-driven parallel robots for industrial applications, 2013, p. 119–34. https://doi.org/10.1007/978-3-642-31988-4_8.

[11] E. Ida, M. Carricato, Static workspace computation for underactuated cable-driven parallel robots, Mech Mach Theory 193 (2024) 105551, https://doi.org/10.1016/j.mechmachtheory.2023.105551.

[12] R. Wang, S. Li, G.S. Member, Y. Li, S. Member, A suspended cable-driven parallel robot with articulated reconfigurable moving platform for schönflies motions, IEEE/ASME Trans Mechatronics 27 (2022) 5173–5184, https://doi.org/10.1109/TMECH.2022.3175217.

[13] Iturralde K., Feucht M., Illner D., Hu R., Pan W., Linner T., et al. Automation in construction cable-driven parallel robot for curtain wall module installation 2022;138. https://doi.org/10.1016/j.autcon.2022.104235.

[14] J.-B. Izard, A. Dubor, P.-E. Hervé, E. Cabay, D. Culla, M. Rodriguez, et al., Large-scale 3D printing with cable-driven parallel robots, Constr Robot 1 (2017) 69–76, https://doi.org/10.1007/s41693-017-0008-0.
[15] K. Vogiatzis, A. Segurson, G.Z. Angeli, Estimating the effect of wind loading on extremely large telescope performance using computational fluid dynamics, Model Syst Eng Astron 5497 (2004) 311, https://doi.org/10.1117/12.551477.
[16] Z. Cui, X. Tang, S. Hou, H. Sun, Research on controllable stiffness of redundant cable-driven parallel robots, IEEE/ASME Trans Mechatronics 23 (2018) 2390–2401, https://doi.org/10.1109/TMECH.2018.2864307.
[17] T.K. Mamidi, S. Bandyopadhyay, A computational framework for the dynamic analyses of cable-driven parallel robots with feed and retrieval of cables, Mech Mach Theory 186 (2023) 29–30, https://doi.org/10.1016/j.mechmachtheory.2023.105338.
[18] H. Yuan, E. Courteille, D. Deblaise, Static and dynamic stiffness analyses of cable-driven parallel robots with non-negligible cable mass and elasticity, Mech Mach Theory 85 (2015) 64–81, https://doi.org/10.1016/j.mechmachtheory.2014.10.010.
[19] D. Gueners, H. Chanal, B.C. Bouzgarrou, Stiffness optimization of a cable driven parallel robot for additive manufacturing, Proc - IEEE Int Conf Robot Autom (2020) 843–849, https://doi.org/10.1109/ICRA40945.2020.9197368.
[20] M. Anson, A. Alamdari, V. Krovi, Orientation workspace and stiffness optimization of cable-driven parallel manipulators with base mobility, J Mech Robot 9 (2017), https://doi.org/10.1115/1.4035988.
[21] S.H. Yeo, G. Yang, W.B. Lim, Design and analysis of cable-driven manipulators with variable stiffness, Mech Mach Theory 69 (2013) 230–244, https://doi.org/10.1016/j.mechmachtheory.2013.06.005.
[22] L. Cuvillon, M.A. Perozo, A. Yiğit, S. Durand, J. Gangloff, Offset-free nonlinear model predictive control for improving dynamics of cable-driven parallel robots with on-board thrusters, Mech Mach Theory 180 (2023) 105141, https://doi.org/10.1016/j.mechmachtheory.2022.105141.
[23] Z. Cui, X. Tang, S. Hou, H. Sun, D. Wang, Optimization design of redundant cable driven parallel robots based on constant stiffness space, IEEE Int Conf Robot Biomimetics 2019 (2019) 1041–1046, https://doi.org/10.1109/ROBIO49542.2019.8961748. ROBIO.
[24] H. Jamshidifar, S. Khosravani, B. Fidan, A. Khajepour, Vibration decoupled modeling and robust control of redundant cable-driven parallel robots, IEEE/ASME Trans Mechatronics 23 (2018) 690–701, https://doi.org/10.1109/TMECH.2018.2793578.
[25] X. Yang, H. Wu, Y. Li, S. Kang, B. Chen, H. Lu, et al., Dynamics and isotropic control of parallel mechanisms for vibration isolation, IEEE/ASME Trans Mechatronics 25 (2020) 2027–2034, https://doi.org/10.1109/TMECH.2020.2996641.
[26] Y. Qin, Q. Chen, C. Ming, Adaptive recursive sliding mode based trajectory tracking control for cable-driven continuum robots, ISA Trans 147 (2024) 501–510, https://doi.org/10.1016/j.isatra.2024.02.016.
[27] J.A. Saglia, N.G. Tsagarakis, J.S. Dai, D.G. Caldwell, A high performance 2-dof over-actuated parallel mechanism for ankle rehabilitation, in: 2009 IEEE Int. Conf. Robot. Autom., IEEE, 2009, pp. 2180–2186, https://doi.org/10.1109/ROBOT.2009.5152604.
[28] D. Gueners, H. Chanal, B.C. Bouzgarrou, Design and implementation of a cable-driven parallel robot for additive manufacturing applications, Mechatronics 86 (2022) 102874, https://doi.org/10.1016/j.mechatronics.2022.102874.
[29] Duan M., Feng J., Liu S. Design, Manufacturing, modelling, and control of a cable-driven parallel robot for additive Manufacturing. 2023 IEEE 19th International Conference on Automation Science and Engineering (CASE), p. 1–6. https://doi.org/10.1109/CASE56687.2023.10260537.
[30] E. Idá, S. Briot, M. Carricato, Natural oscillations of underactuated cable-driven parallel robots, IEEE Access 9 (2021) 71660–71672, https://doi.org/10.1109/ACCESS.2021.3071014.